Shear-induced ordering of nano-pores and instabilities in surfactant mesh phases

Pradip K. Bera[1a], Vikram Rathee[1ab], Rema Krishnaswamy[1c] and A.K. Sood[1*]

[1] *Department of Physics, Indian Institute of Science, Bangalore 560012, India*

(Dated: August 20, 2020)

Abstract

Mixed surfactant systems show many interesting phases such as the random mesh phase consisting of a disordered array of defects (water-filled nano-pores in the bilayers). The present study addresses the non-equilibrium phase transition of the random mesh phase under shear to an ordered mesh phase with high degree of coherence between defects in three dimensions. In-situ small-angle synchrotron X-ray diffraction under different shear stress conditions shows sharp Bragg peaks in X-ray diffraction, successfully indexed to the rhombohedral lattice with the R$\bar{3}$m space group symmetry. The ordered mesh phase shows isomorphic twinning and buckling at higher shear stress. Our experimental studies bring out rich phase transitions in concentrated mixed surfactant systems hitherto not well explored and provide motivation for a quantitative understanding.

[a] These authors contributed equally to this work.

[b] Present address: Okinawa Institute of Science and Technology Graduate University, Okinawa, Japan

[c] Present address: School of Arts and Sciences, Azim Premji University, Bangalore, 560100, India

[*] asood@iisc.ac.in

I. INTRODUCTION

Mesh phases are liquid crystalline phases formed in ionic as well as non-ionic mixed surfactant systems, consisting of 1D stack of bilayers with water-filled pores or curvature defects. Depending on the correlation of these defects, the phase can be distinguished as random mesh phase (L_α^D) if the defects exhibit a liquidlike ordering and ordered mesh phase if the defects are correlated across the bilayers locked into a three dimensional lattice. These can be further classified as tetragonal or rhombohedral ($R\bar{3}m$) mesh phase, depending on their structural symmetry [1–3]. As a simple manifestation, the mesh phase is structurally similar to the adjacent lamellar phase which occurs at higher surfactant concentrations and topologically similar to the preceding hexagonal phase formed at lower surfactant concentrations. However, non-uniform mean curvature in the mesh phase is in sharp contrast with the hexagonal or lamellar phase [4, 5]. Extensive studies on the equilibrium phase behaviour of lyotropic surfactant systems have established that the spontaneous formation of the defects/pores in the mesh phase and their long-range ordering across the stack of the bilayers require a balancing of the head group interactions and the chain flexibility, particularly through the addition of a third component to a binary surfactant-water mixture [2, 6–13]. Similarly, the perforated bilayers in lipid-water systems form intermediate phases due to incorporation of proteins into the pores [14].

The kinetics of the mesh phase to the lamellar phase transition is well understood in equilibrium, and there have been many recent reports which indicate the role of counterions and temperature [1, 15–19]. Despite the structural similarity between the unperforated lamellar phase and the mesh phase, the dynamical behaviour of the mesh phase under shear stress is less understood. In the context of bilayers, it is known that the external flow modifies the amphiphilic interfaces resulting in transitions such as rolling of bilayers into spherulite known as onions [20–22]. The transitions in bilayer systems have been attributed to suppression of thermal undulations due to imposed shear stress causing hydrodynamical instabilities which occur above a critical shear rate (inversely proportional to the bilayer spacing), and thus are observed only in dilute liquid crystalline phases [23, 24]. In comparison, in concentrated surfactant systems, above the Kraft temperature, shear induced reversible transition from bilayers to crystalline phase is observed at intermediate shear rates originating from re-distribution of the counterions [25]. Similarly, shear induced unbinding of counterions

is observed in other bilayer forming or multilamellar vesicles phase [26]. Also, an increase in alignment of the randomly oriented crystallites, bilayers or cylinders over macroscopic dimensions in the plane of shear as well as a transition from random mesh phase to the onion phase under shear have been observed [22, 27]. Notably, the transition to the onion phase is preceded by a change in orientation of the bilayers.

Here, we bring out a few unexplored aspects of flow behavior of the mesh phases formed in mixed cationic-anionic surfactant systems. Time resolved Rheo-SAXS measurements allow us to follow the temporal evolution of the X-ray diffraction peaks corresponding to different lattice planes of defects in the bilayers. A reorientation of the bilayers in L_α^D phase is always observed under shear with the bilayers stacked along the shear plane ($\mathbf{V}$-$\nabla\mathbf{V}$ plane) which is identified as the a-orientation. Intriguingly, further shearing reveals two distinct structural transitions depending on the separation between the bilayers. At lower surfactant concentrations (larger bilayer separation), the a-oriented bilayers transform to an onion phase, whereas, at higher surfactant concentrations (smaller bilayer separation), a transition to $R\bar{3}m$ phase is observed. The L_α^D phase to $R\bar{3}m$ phase transition occurs through the onset of correlation of the nano-pores across the bilayers before they lock into a 3D rhombohedral lattice. This is followed by the shear-induced isomorphic twinning and buckling transition of the ordered mesh phase ($R\bar{3}m$) due to the hydrodynamic instability.

II. EXPERIMENTAL DETAILS

A. Materials

Surfactants cetyltrimethylammonium bromide (CTAB) and cetylpyridinium chloride (CPC) from Sigma Aldrich were used without further purification. Sodium-3-hydroxy-2-naphthoate (SHN) was prepared by adding an equivalent amount of an aqueous solution of sodium hydroxide (NaOH) to an ethanol solution of 3-hydroxy-2-naphthoic acid (HNA). Ternary solutions of surfactant, SHN and water were prepared with deionized water (resistivity $\sim$ 18.2 MΩ.cm) for the total weight fraction of surfactant + SHN ($\phi = (\text{Surfactant} + \text{SHN})/(\text{Surfactant} + \text{SHN} + H_2O)$) at the desired molar ratio of the two components ($\alpha = \frac{[\text{SHN}]}{[\text{Surfactant}]}$) [2]. In equilibrium, the counterion SHN is known to be adsorbed at the micelle-water interface [2, 3, 8], thus decreasing the spontaneous curvature

of the micellar aggregates formed by CTAB or CPC, to transform the cylindrical micelles to bilayers as α approaches 1. The detailed equilibrium phase diagrams of these systems ([8]) have shown random and ordered mesh phases over a wide range of surfactant concentration ($0.2 < \phi < 0.7$). In our present experiments, the value of α was fixed at 1 for CTAB-SHN-water system and 0.5 for CPC-SHN-water system. The samples were well sealed and left in an oven at 40° C for more than 2 weeks to equilibrate. All the measurements were done with the freshly loaded sample.

B. Rheo-SAXS experiments

We have used time-resolved small-angle X-ray scattering (SAXS) setup coupled with Haake-Mars rheometer at the P10 beamline of the PETRA III synchrotron [see Fig. S1 in the Supplemental Material [28]] [29]. The sample chamber was fitted with a Peltier based temperature controller and a humidity controller along with nitrogen flow. The synchrotron X-ray beam was deflected vertically and passed through the sample. The X-ray diffraction patterns were recorded on a Pilatus 300 K detector with the varying exposure time of 10-50 seconds. For parallel plate (PP) vespel geometry (DuPont, diameter 35 mm), due to high absorbance, the sample thickness was chosen to be 1 mm and the X-ray beam was in velocity gradient direction at a fixed position 13 mm from the plate centre. The detector was placed parallel to the velocity-vorticity plane, at a distance 1000 mm from the sample. For the Couette glass geometry (with a diameter of 29 mm for the inner cylinder and a gap of 4 mm), the sample height was 5.5 mm, and the X-ray beam was along the vorticity direction with the detector plane parallel to the velocity-velocity gradient plane. The position of the beam was varied in Couette's radial direction by slowly translating the motorized stage of the rheometer.

C. Rheo-SALS experiments

In-situ depolarized small-angle light scattering (SALS) measurements were performed along with rheology in a stress-controlled rheometer (MCR 102, Anton Paar) fitted with a temperature controller [see Fig. S1 in the Supplemental Material [28]]. Parallel plate (PP) glass geometry of diameter 43 mm was used with 1 mm sample thickness. The laser beam

(wavelength of 658 nm) was in the velocity gradient direction at a fixed position 15 mm from the plate center. SALS images on the white screen (parallel to the velocity-vorticity plane) were recorded by an 8-bit color CCD camera (Lumenera, 0.75C, 1200×980 pixels) fitted with a PENTAX TV Lens of focal length 12 mm.

III. RESULTS AND DISCUSSION

Otherwise stated, here all the measurements were done at 30° C (above the Kraft temperature 25° C) with the PP vespel geometry having sample thickness of 1 mm. We have estimated the size of the water-filled defects ($\sim \sqrt[3]{\text{defect volume}}$) to be in the range from 4.5 nm to 6 nm [see section-A in the Supplemental Material [28]] and hence justifying calling the defects as nano-pores.

A. Random mesh phase ($\mathbf{L}_\alpha^D$) to onion phase transition under shear

We start with CTAB-SHN-water system for $\phi < 0.5$ and $\alpha = 1$ for which the flow curve is shown in Fig. 1(a), recorded with the waiting time at each stress to be 30 sec. We point out that these flow curves are not in a steady state as the system evolves with time under stress. It can be seen that the lamellar phase exhibits a typical shear thinning behavior where viscosity (η) decreases with shear rate or stress. At smaller shear rates, the lamellae sheets flow pass over each other resulting in a sharp decrease before showing an inflection point, followed by another shear thinning region. In the reverse run, we observe only shear thinning behavior suggesting that the observed structural changes are not shear reversible. Since flow curve measurements are time averaged over several seconds at a particular shear rate, time resolved rheology reveals temporal evolution of viscosity at a constant shear rate. Figure 1(b),(f) show the evolution of η at a constant shear rate ($\dot{\gamma}$) of 10 s^{-1}, for two different volume fractions $\phi = 0.3$ and 0.4 respectively at $\alpha = 1$. For both values of ϕ, η shows a minimum at $t \sim 10$ s and then increases to a high value. For $\phi = 0.3$, without shear, the X-ray diffraction pattern consists of an isotropic Bragg ring due to the randomly oriented lamellae having d-spacing $d_l = 9.60$ nm [Fig. 1(c)]. Here, we do not observe the diffuse scattering peak due to the lack of in-plane correlation between nano-pores. Before $t = 1000$ s, no significant change in the X-ray diffraction pattern is observed [Fig. 1(d)].

However, a six-fold hexagonal shaped pattern is observed [Fig. 1(e)] in the steady state after $t = 1000$ s, suggesting a 2D hexagonal close pack ordering of onions under shear. For $\phi = 0.4$, without shear, the observed unoriented lamellae [Fig. 1(g)] has a d-spacing $d_l = 7.30$ nm and the nano-pores have in-plane correlation length $d_d = 6.93$ nm [Supplemental Material [28], Table S1]. For $t \geq 10$ s, a-orientation of the bilayers [30] is observed where the lamellar peak is sharp along the vorticity direction (in the $\nabla\times\mathbf{V}$ direction or $\mathbf{q}_\perp$ direction) and the diffuse scattering peak becomes sharp along the flow direction (in the $\mathbf{V}$ direction or $\mathbf{q}_\parallel$ direction), indicating bilayer planes stacked parallel to the $\mathbf{V}$-$\nabla\mathbf{V}$ plane (the shear-plane) [Fig. 1(h)]. The observed decrease in viscosity corresponding to the a-orientation indicates that the bilayers offer less resistance to shear in this configuration. After $t = 1000$ s, a sharp isotropic Bragg ring is observed suggesting the formation of the onion phase under shear [Fig. 1(i)]. Further, we have used the in-situ small-angle light scattering (Rheo-SALS) to confirm the L_α^D phase to onion phase transition, by observing a four-lobed clover-leaf pattern, a signature of the onion or multilamellar vesicles, under the depolarized SALS [22]. The Rheo-SALS measurements were performed in the VH (polarizer $\perp$ analyzer) configuration. Figure 2 shows the evolution of Rheo-SALS patterns obtained during the stress relaxation measurement of L_α^D phase for $\phi = 0.4$ at $\dot{\gamma} = 10$ s^{-1}. The time evolution of η is the same as in Fig. 1(f) (data not shown). At $t \sim 10$ s, the isotropic pattern [Fig. 2(a)] changes to an anisotropic pattern [Fig. 2(b)], oriented along the $\mathbf{q}_\perp$ direction indicating the flow alignment of bilayers parallel to the shear-plane. After $t = 500$ s, the expected four-lobed clover-leaf pattern associated with the onion phase appears [Fig. 2(c)]. Our SAXS and SALS measurements indicate hexagonal close packing of the onions under shear. The increase in η is result of the transition from a well separated lamellae to closely packed spherulite. After 1000 s, the observed fluctuations in the η is possibly due to the onions' re-arrangements or variation in the size of these onions [31]. Though L_α^D phase to onion phase transition under shear is a well studied phenomenon [22], the noteworthy aspect of the present study is the crucial role of curvature defects in driving this transition that has not been addressed in earlier reports. We show that the bilayers transform to onions or spherulites only for a low density of curvature defects in the plane of the bilayers. A higher defect density with a correlation length > 7 nm induces a 3D ordering of defects to preclude the formation of an onion phase.

B. Shear-induced 3D ordering of nano-pores in L_α^D phase

The concentrated L_α^D phase formed in the CTAB-SHN-water system at $\phi = 0.5$ and $\alpha = 1$, demonstrates L_α^D phase to $R\bar{3}m$ phase transition under shear. On applying a constant shear rate $\dot{\gamma} = 50\ s^{-1}$, η of the L_α^D phase decreases with time and it reaches the steady state after $t \sim 200$ s [Fig. 3(a)]. Figure 3(b–f) show the temporal evolution of the X-ray diffraction pattern. In the quiescent state, the X-ray diffraction pattern [Fig. 3(b)] reveals two Bragg rings with their q ratio 1:2 (characteristic of an unaligned lamellar phase), with $d_l = 5.49$ nm [Table I]. As expected in a random mesh phase, the diffuse isotropic ring observed at a smaller angle confirms the existence of liquid-like correlated nano-pores (water-filled) in the plane of the bilayer with an in-plane correlation length $d_d = 7.67$ nm. The nearly isotropic Bragg rings corresponding to the lamellar spacing of bilayers and the liquid-like correlation of the in-plane nano-pores evolve to the well aligned anisotropic diffraction pattern at $t \sim 50$ s, revealing the a-oriented state of the bilayers [Fig. 3(c)]. The occurrence of the diffuse scattering peaks as arcs azimuthally centred at $\mathbf{q}_\parallel \sim 0$ suggests an absence of the trans-bilayer correlation of the nano-pores. Notably, at $t \sim 515$ s, the azimuthal intensity profile of the diffuse scattering peak shows a splitting away from $\mathbf{q}_\parallel = 0$ [Fig. 3(e)], suggesting the onset of long range correlation of the nano-pores across the bilayers favoring the formation of a 3D ordered structure. At $t \sim 850$ s [Fig. 3(f)] a few more peaks appear in the X-ray diffraction pattern, with no further change upon shearing up to 1000 s indicating a steady state. All the partially oriented Bragg reflections of this diffraction pattern could be indexed to a rhombohedral lattice with the space group $R\bar{3}m$ [Table I] with lattice parameters $a = 8.68$ nm and $c = 15.93$ nm, coexisting with the L_α^D phase. The lamellar reflection of the L_α^D phase overlaps with the (003) reflection of $R\bar{3}m$ phase (lamellar periodicity $\sim c/3 = 5.31$ nm) and its coexistence with $R\bar{3}m$ phase in the final steady state is inferred from the diffuse arcs azimuthally centred at $\mathbf{q}_\parallel \sim 0$. We have chosen the indexing scheme where the first reflection which overlaps with the diffuse scattering peak from the nano-pores, is indexed as (101) and the third reflection which lies on the $\mathbf{q}_\perp$ axis as the (003) reflection. As seen from Table I, the second reflection which appears as the shoulder of the (003) reflection can be indexed as the (012) reflection. Moreover the (110) reflection corresponding to scattering from the in-plane nano-pores of the bilayers lie along $\mathbf{q}_\parallel$, further confirming the robustness of our indexation to the diffraction peaks of the $R\bar{3}m$ structure.

The structure of the shear-induced R$\bar{3}$m phase could be modelled as an ordered mesh phase with ABC stacking of 3-connected rods [8]. Moreover, the lattice parameters obtained for the shear induced R$\bar{3}$m phase is identical to that obtained for the equilibrium R$\bar{3}$m phase at a surfactant concentration of $\phi = 0.53$. The value of micellar radius (r_m) determined from this model for the above lattice parameters is 2.10 nm, consistent with the equilibrium value reported in Ref. [8]. We propose that the decrease in viscosity η during this transition is due to both, the persistence of the a-orientation of the bilayers that offer a low resistance to shear as well as the 3D ordering of the nano-pores providing the passage for the liquid to pass through the connected pores.

To ascertain that the shear-induced L_α^D phase to R$\bar{3}$m phase transition is generic, at least to other cationic-anionic mixed surfactant systems, we have also studied the concentrated L_α^D phase (with $d_l = 5.13$ nm and $d_d = 6.50$ nm) formed in CPC-SHN-water system ($\phi = 0.55$ and $\alpha = 0.5$) [3]. In this case also, we have observed a similar transition from L_α^D phase to R$\bar{3}$m phase [see section-B in the Supplemental Material [28]]. The viscosity η decreases with time but reaches the steady state after $t \sim 20$ s [Supplemental Material [28], Fig. S3(a)], in a comparatively short period of time (compared to the CTAB-SHN-water system shown in Fig. 3). Under shear, the L_α^D phase goes to the coexistence of two R$\bar{3}$m phases with lattice parameters $a1 = 8.39$ nm; $c1 = 14.79$ nm; $a2 = 8.27$ nm; $c2 = 14.28$ nm [Supplemental Material [28], Table S2].

C. Mechanism of shear-induced ordering of the nano-pores and the L_α^D phase to R$\bar{3}$m phase transition

The shear-induced R$\bar{3}$m phase obtained in two different systems on applying a constant shear rate indicates that this transition is a general feature of concentrated random mesh phases. The distinguishing feature governing the kinetics of the L_α^D phase to R$\bar{3}$m phase transition at a constant shear rate, that may be identified in both these systems from the time resolved Rheo-SAXS measurements, is the a-orientation of the lamellae prior to the appearance of the sharp (101) reflection corresponding to the 3D ordering of nano-pores. In the presence of thermal undulations, the a-orientation of bilayers in the lamellar phase is usually preferred at high shear rates since the suppression of thermal undulations under shear is lower in the a-orientation in comparison with the c-oriented state (where the bilayer

planes are stacked parallel to the $\mathbf{V}$-$\nabla\times\mathbf{V}$ plane) [32]. In the simplest model [33, 34], as the bilayers of L_α^D phase are formed by in-plane array of rods, shear is likely to increase the average length of the cylinders forming the 2D hexagonal mesh when the bilayers align along the shear plane ($\mathbf{V}$-$\nabla\mathbf{V}$ plane). The hexagonal pores have two distinct contributions to the curvature energy; from the radius of the micellar cylinders, corresponding to a curvature C_1 and the radius of the pore that may be visualized as a circle formed by the in-plane array of rods with a curvature (C_2). The free energy per unit area of a monolayer, therefore, is given by $E = (\kappa/2)(C_1 + C_2 - C_0)^2 + \bar{\kappa}C_1C_2$ where C_0 is the spontaneous curvature, and κ, $\bar{\kappa}$ are the rigidity and Gaussian curvature constants, respectively [34]. A shear driven increase in the length of the rods implies an increase of the radius of the in-plane nano-pores, leading to a lower curvature and consequently a lower curvature energy. The lower curvature energy favors the increment of the in-plane as well as the trans-bilayer correlation length of the nano-pores. Further, we propose that the locking of the nano-pores into a 3D lattice occurs when the in-plane correlation length of the nano-pores (d_d) is larger than the bilayer periodicity (d_l). A comparison can be drawn here with respect to the equilibrium phase behavior of the system (CTAB-SHN-water system, $\alpha = 1$), where the L_α^D phase to $R\bar{3}m$ phase transition is observed with decreasing water content (for $\phi > 0.5$). By defining the in-plane periodicity ratio (Γ) which is determined from the ratio of d_d (or lattice parameter a in case of $R\bar{3}m$) to the bilayer separation d_l for the L_α^D phase (or lattice parameter $c/3$ in case of $R\bar{3}m$), we find that when the surfactant volume fraction ϕ increases from 0.5 to 0.53, Γ increases from a value of 1.2 in L_α^D phase to 1.4 in $R\bar{3}m$ phase. A crucial aspect favoring our argument would be an increase in d_d with shear observed from the diffuse scattering peak positions. However, domains of L_α^D with an increased d_d is not observed in our experiments possibly because the strong flow imposed on the sample at a high shear rate, smears out the diffraction pattern from these domains, giving rise to a broad and diffuse scattering peak. Nevertheless, it should be noted that an increase in pore size at a constant water content (ϕ) implies that water from the inter-bilayer region will enter into the nano-pores, thus decreasing the bilayer separation. Hence the observed decrease in the lamellar periodicity by ~ 3 Åunder shear reinforces the proposed shear-induced increase in average pore size. Further, the consequent increase in Γ from 1.3 to 1.6 for the shear-induced $R\bar{3}m$ phase is consistent with the increase in Γ observed for L_α^D phase to $R\bar{3}m$ phase transition on decreasing water content [8]. It is noteworthy that the L_α^D phase to $R\bar{3}m$ phase transition is absent at lower surfactant volume

fractions $\phi < 0.5$ as explained above. A robust conclusion that emerges from our studies on the concentrated random mesh phase is that a shear-induced ordering of the membrane nano-pores occludes the formation of onion phases.

D. Plastic deformation of R$\bar{3}$m phase during flow

We will now present the effects of shear flow on the randomly oriented crystallites of the R$\bar{3}$m phase for different values of ϕ [see section-C in the Supplemental Material [28] for the SALS and the SAXS measurements with the equilibrium R$\bar{3}$m phase]. Figure 4(a) shows the stress-controlled flow curve of R$\bar{3}$m phase (CTAB-SHN-water, $\phi = 0.53, \alpha = 1$) with a stepwise increment in shear stress with 200 s waiting time at each data point. The diffraction pattern of the randomly aligned sample at $\sigma = 0$ Pa [Fig. 4(b)] progressively transforms to the perfectly aligned sample (a-oriented state) at $\sigma = 590$ Pa with $\dot{\gamma} \sim 1$ s^{-1} [Fig. 4(c),(d)]. The X-ray diffraction pattern of the perfectly aligned phase [Fig. 4(d)] has four diffuse arcs in (101), (012) Bragg rings and has two concentrated arcs in the (003) Bragg ring, consistent with the rotational symmetry of reciprocal lattice points of R$\bar{3}$m [35]. At $\sigma = 660$ Pa (corresponding $\dot{\gamma} \sim 100$ s^{-1}), six arcs are observed in (101), (012) Bragg rings, respectively, which we propose are due to buckling with two different states of orientation (i.e. presence of two directors) [Fig. 4(e)], consistent with the observed star-like pattern in the Rheo-SALS measurement [see section-D in the Supplemental Material [28]]. In the Rheo-SALS, the pattern is wide in two different directions (nearly orthogonal) which can be interpreted that the system has two preferred directions of bilayer orientations during flow. The lattice parameters of R$\bar{3}$m remain same before and after the buckling [see Table II]. For $\sigma > 700$ Pa, a very rapid avalanche flow is observed.

To probe this transition at different positions in the shear gradient direction in PP geometry, the X-ray has to pass through the sample at an angle to the vorticity direction which would not be feasible in the present scattering geometry. In order to overcome this difficulty, we have used the Couette geometry as discussed below. The X-ray beam was translated along the gradient direction to place the beam at different positions (g_x) in the Couette gap. In the PP geometry, the structural transition occurs at $\dot{\gamma} \sim 1$ s^{-1}, thus here we have followed the temporal evolution of the X-ray diffraction patterns under stress relaxation measurement at $\dot{\gamma} = 1$ s^{-1} [Fig. 5]. The viscosity shows a monotonic decay up to ~ 100 s

and then fluctuates about 20 Pa-s in the steady state. The X-ray diffraction patterns were recorded after 700 s. Remarkably, an unexpected rich sequence of orientational transition accompanies the coexistence of two R$\bar{3}$m phases as discussed below. The sharp isotropic Bragg rings in the quiescent state transform to the aligned diffraction pattern (c-oriented state). The X-ray diffraction patterns for four different g_x are showing the coexistence of two R$\bar{3}$m phases with different lattice parameters [Table III]. The relative orientation of these two R$\bar{3}$m phases changes with g_x as the incident X-ray beam is taken from the stator towards the rotor.

We have also performed the shear rate relaxation measurements on an unaligned R$\bar{3}$m phase in Couette geometry [Fig. 6]. For $\sigma < 100$ Pa, the system flows with a partially c-oriented R$\bar{3}$m throughout the gap between shearing cylinders [Fig. 6(c)]. On applying high stress ($\sigma = 100$ Pa), the diffraction pattern shows several Bragg rings [Fig. 6(b)]. Coexistence of two R$\bar{3}$m phases with different lattice parameters [Table IV] is observed in all the diffraction patterns for all g_x, except for $g_x = 1.2$ mm (here only the starting R$\bar{3}$m phase is observed). The relative orientation of these two R$\bar{3}$m changes with g_x as one goes from stator to the rotor. The presence of six or eight arcs in (101), (012) Bragg rings near the inner static cylinder [Fig. 6(b)] suggests buckling of R$\bar{3}$m structure with two different states of the orientation of nano-crystallites with the same lattice parameters.

Now we correlate the modulation in the X-ray diffraction to the domains' orientation deep inside the sample under shear (for example part (d) and (e) of Fig. 4). At a moderate shear rate R$\bar{3}$m phase has a-aligned state with all layers facing towards vorticity direction and the X-ray diffracting in a perpendicular direction to the layer normal will show two very strong arcs in the (003) Bragg ring and four arcs in (012), (101) Bragg rings due to lattice symmetry of R$\bar{3}$m. At a high shear rate, few layers still retain the a-oriented state but others reorient themselves at a certain angle ($\sim 45^\circ$) with the vorticity direction, giving rise to more than four arcs in (012), (101) Bragg rings. The absence of many arcs in the (003) Bragg ring can be due to the fact that the (003) diffraction has only two-fold symmetry and the reoriented layers can easily miss it due to the finite angle with the shear gradient direction. This scenario is depicted in Fig. S6 in the Supplemental Material [28]. This model has been used to explain the small-angle scattering data from the Kraton-type block copolymers during tensile deformation where four arcs were observed in place of two in the Bragg ring corresponding to the spacing between cylinders [36].

The concentrated R$\bar{3}$m phase (CTAB-SHN-water, $\phi = 0.60, \alpha = 1$) also shows the buckling and the coexistence of two R$\bar{3}$m phases under shear as discussed below. The stress-controlled flow curve is obtained by varying the stress in the range 700 Pa to 1700 Pa in 30 logarithmic steps with a waiting time of 50 s per data point [Fig. 7(a)]. The unaligned diffraction pattern transforms to an aligned pattern at $\sigma = 1133$ Pa [Fig. 7(b)]. Four diffuse arcs appear on the (101) Bragg ring of the R$\bar{3}$m. For $\sigma = 1400$ Pa (corresponding $\dot{\gamma} \sim 1$ s^{-1}), six arcs are observed on the (101) Bragg ring as well as the azimuthal spread of the arcs become smaller [Fig. 7(c)]. For $\sigma = 1600$ Pa (corresponding $\dot{\gamma} \sim 10$ s^{-1}), two R$\bar{3}$m phases with different lattice parameters appear [Fig. 7(d)]. The two sets of lattice parameters $a = 8.13$ nm, $c = 13.80$ nm, and $a = 7.69$ nm, $c = 13.80$ nm [see Table V] show lower values compared to the equilibrium lattice parameters ($a = 8.30$ nm, $c = 14.10$ nm). We have followed the temporal evolution of the X-ray diffraction pattern during the stress relaxation measurement at 1 s^{-1} [Fig. 8(a)]. Again the sharp isotropic Bragg rings in the quiescent state [Fig. 8(b)] transform to an aligned diffraction pattern at $t \sim 70$ s [Fig. 8(c)]. The oriented (003) reflection along the vorticity direction indicates the transition to the a-oriented state. At $t = 75$ s, eight diffuse scattering arcs lying on (101), (012) Bragg rings are observed [Fig. 8(d)] which is due to buckling of the R$\bar{3}$m. At $t = 80$ s [Fig. 8(e)], additional Bragg rings start appearing indicating the onset of another structural transition. The X-ray diffraction pattern obtained at $t = 550$ s shows the stable pattern in the steady-state having a few additional reflections. Eight arcs are seen on different Bragg rings orientated in the same azimuthal direction. Considering all the Bragg rings, the diffraction pattern can be indexed to two R$\bar{3}$m phases with different lattice parameters [see Table VI].

IV. CONCLUSIONS

To summarize, we have shown that at relatively low concentration, L_α^D of the CTAB-SHN-water system goes to the onion phase under shear, similar to the previously reported studies [22]. During this transition, the system viscosity increases and remains high in the onion phase. The high concentrated L_α^D phase transforms to the R$\bar{3}$m phase under the shear flow where the nano-pores achieve and maintain their long-ranged in-plane as well as out-of-plane correlations in the non-equilibrium state. A similar transition is also observed in the CPC-SHN-water system. We argue that under shear the transition from the random

mesh phase to the ordered mesh phase is likely to be a more general feature of the mesh phases and is expected to occur whenever an ordered mesh phase is present adjacent to the random mesh phase in the equilibrium phase diagram. The absence of a shear induced transition from the random mesh phase to the ordered mesh phase, in the earlier studies on different mixed surfactant systems can thus be attributed to the absence of an ordered mesh phase in the equilibrium phase diagram of those systems [22, 37]. A crucial point to be noted is that the equilibrium phase transition from a random mesh phase to an ordered mesh phase occurs with decreasing water content if the correlation length of the defects increase with surfactant's weight fraction (ϕ). Intriguingly, here in our studies, the lamellar d-spacing decreases under shear only at higher values of ϕ where the transition appears, providing us with a clue to the origin of this transition. We propose that the decrease in the bilayer separation under shear increases the strength of the interaction potential due to the in-plane modulations (from the mesh-like aggregates forming the bilayer), across the bilayers locking them into a 3D lattice. This decrease in lamellar spacing can arise possibly from the squeezing out of the water from the adjacent bilayers, or alternately due to the increase in the average separation between the defects. Plastic flow of $R\bar{3}m$ phase shows isomorphic twinning transition having slightly different lattice parameters, giving rise to the splitting of the Bragg peaks and the six or eight points modulation of the Bragg rings. The in-situ SALS measurement shows star-like pattern for this transition. We propose that the star-like pattern in the SALS and the modulation of the (101), (012) Bragg rings with more than four arcs is due to different states of the director's orientation. This can be visualized as buckling of the ordered mesh phase under shear. We cannot rule out completely the other possibility that the bilayers of the ordered mesh phase under shear roll into the multi-lamellar cylinders arranged in hexagonal or tetragonal array giving rise to 6 or 8 arcs in the (101), (012) Bragg rings. In that case, large fluctuations in the viscosity even after a long time (Fig. 6, 8) can be due to the changing orientation of these cylinders under shear resulting in oscillations/fluctuations. The decrease in viscosity, however, does not support the formation of cylinders since rolling up of lamellae into cylinders usually increases the resistance to flow and results in increased viscosity [38]. To this end, we have performed the Rheo-SAXS measurement of low concentrated $R\bar{3}m$ phase using the Couette geometry to probe the directionality of the twinning and buckling with respect to the flow. The concentration was so chosen as to avoid breaking of the glass Couette geometry due to

high viscosity. With the Couette geometry we have observed c-oriented state of the R$\bar{3}$m phase at a low value of shear rate and then observed isomorphic twinning of R$\bar{3}$m phase with substantial variation in the relative orientation of the directors as one goes from stator to the rotor. This suggests that the buckling angle can vary in velocity gradient direction and also the crystallites corresponding to different directors may have different lattice parameters. We further surmise that the decrease in the lattice parameters under shear leads to the expulsion of the excess solvent creating a lubrication layer near the moving plate. Hence the structural transitions discussed above brings about a regime of total wall slip and an accompanying avalanche flow due to the sharp increase in the shear rate. We hope that our experimental studies will motivate quantitative theoretical understanding of shear induced transitions in concentrated mixed surfactant systems.

V. CONFLICTS OF INTEREST

There are no conflicts to declare.

VI. ACKNOWLEDGEMENTS

A.K.S. thanks Department of Science and Technology (DST), India for the support under Year of Science Professorship. R. K. thanks DST, India for the Ramanujan Fellowship. V.R. thanks the Council for Scientific and Industrial Research (CSIR), India for the Senior Research Fellowship. P.K.B. thank University Grants Commission (UGC), India for the Senior Research Fellowship. We thank DST, India for financial assistance through DST-DESY Project (I-20140281) to use the Synchrotron Beam-time. We acknowledge DESY (Hamburg, Germany), a member of the Helmholtz Association HGF, for the provision of experimental facilities. Parts of this research were carried out at PETRA III and we thank Dr. Michael Sprung, Dr. Alexey Zozulya, and Eric Stellamanns for assistance in using the P10 beamline.

[1] P. Kekicheff and G. J. T. Tiddy, "Structure of the intermediate phase and its transformation to lamellar phase in the lithium perfluorooctanoate/water system," *The Journal of Physical*

Chemistry, vol. 93, no. 6, pp. 2520–2526, 1989.

[2] R. Krishnaswamy, S. K. Ghosh, S. Lakshmanan, V. A. Raghunathan, and A. K. Sood, "Phase behavior of concentrated aqueous solutions of cetyltrimethylammonium bromide (CTAB) and sodium hydroxy naphthoate (SHN)," *Langmuir*, vol. 21, no. 23, pp. 10439–10443, 2005.

[3] S. P. Gupta and V. A. Raghunathan, "Controlling the thermodynamic stability of intermediate phases in a cationic-amphiphile–water system with strongly binding counterions," *Physical Review E*, vol. 88, no. 1, p. 012503, 2013.

[4] M. E. Cates and S. J. Candau, "Statics and dynamics of worm-like surfactant micelles," *Journal of Physics: Condensed Matter*, vol. 2, no. 33, p. 6869, 1990.

[5] M. C. Holmes and M. S. Leaver, "Intermediate phases. In Bicontinuous Liquid Crystals (Surfactant Science Series)," *Lynch, M. L., Spicer, P. T., Eds.; Taylor & Francis: Boca Raton*, vol. 127, pp. 15–39, 2005.

[6] S. S. Funari, M. C. Holmes, and G. J. T. Tiddy, "Microscopy, X-ray diffraction, and NMR studies of lyotropic liquid crystal phases in the C22EO6/water system: a new intermediate phase," *The Journal of Physical Chemistry*, vol. 96, no. 26, pp. 11029–11038, 1992.

[7] M. Leaver, A. Fogden, M. Holmes, and C. Fairhurst, "Structural Models of the R$\bar{3}$m Intermediate Mesh Phase in Nonionic Surfactant Water Mixtures," *Langmuir*, vol. 17, no. 1, pp. 35–46, 2001.

[8] S. K. Ghosh, R. Ganapathy, R. Krishnaswamy, J. Bellare, V. A. Raghunathan, and A. K. Sood, "Structure of mesh phases in a cationic surfactant system with strongly bound counterions," *Langmuir*, vol. 23, no. 7, pp. 3606–3614, 2007.

[9] E. H. Lucassen-Reynders, J. Lucassen, and D. Giles, "Surface and bulk properties of mixed anionic/cationic surfactant systems in equilibrium surface tensions," *Journal of Colloid and Interface Science*, vol. 81, no. 1, pp. 150–157, 1981.

[10] C. Manohar, U. R. K. Rao, B. S. Valaulikar, and R. M. Lyer, "On the origin of viscoelasticity in micellar solutions of cetyltrimethylammonium bromide and sodium salicylate," *Journal of the Chemical Society, Chemical Communications*, no. 5, pp. 379–381, 1986.

[11] E. W. Kaler, K. L. Herrington, A. K. Murthy, and J. A. N. Zasadzinski, "Phase behavior and structures of mixtures of anionic and cationic surfactants," *The Journal of Physical Chemistry*, vol. 96, no. 16, pp. 6698–6707, 1992.

[12] M. T. Yatcilla, K. L. Herrington, L. L. Brasher, E. W. Kaler, S. Chiruvolu, and J. A. Zasadzinski, "Phase behavior of aqueous mixtures of cetyltrimethylammonium bromide (CTAB) and sodium octyl sulfate (SOS)," *The Journal of Physical Chemistry*, vol. 100, no. 14, pp. 5874–5879, 1996.

[13] M. J. Blandamer, B. Briggs, P. M. Cullis, and J. B. F. N. Engberts, "Titration microcalorimetry of mixed alkyltrimethylammonium bromide surfactant aqueous solutions," *Physical Chemistry Chemical Physics*, vol. 2, no. 22, pp. 5146–5153, 2000.

[14] R. P. Rand and V. Luzzati, "X-ray diffraction study in water of lipids extracted from human erythrocytes: the position of cholesterol in the lipid lamellae," *Biophysical Journal*, vol. 8, no. 1, pp. 125–137, 1968.

[15] V. A. Raghunathan, "Mesh phases of surfactant-water systems," *Journal of the Indian Institute of Science*, vol. 88, no. 2, pp. 197–210, 2012.

[16] V. Luzzati, H. Mustacchi, A. Skoulios, and F. Husson, "La structure des colloïdes d'association. I. Les phases liquide–cristallines des systèmes amphiphile–eau," *Acta Crystallographica*, vol. 13, no. 8, pp. 660–667, 1960.

[17] P. Kékicheff, "From cylinders to bilayers: A structural study of phase transformations in a lyotropic liquid crystal," *Molecular Crystals and Liquid Crystals*, vol. 198, no. 1, pp. 131–144, 1991.

[18] C. E. Fairhurst, M. C. Holmes, and M. S. Leaver, "Structure and morphology of the intermediate phase region in the nonionic surfactant C16EO6/water system," *Langmuir*, vol. 13, no. 19, pp. 4964–4975, 1997.

[19] M. C. Holmes, "Intermediate phases of surfactant-water mixtures," *Current Opinion in Colloid and Interface Science*, vol. 3, no. 5, pp. 485–492, 1998.

[20] O. Diat, D. Roux, and F. Nallet, "Effect of shear on a lyotropic lamellar phase," *Journal de Physique II*, vol. 3, no. 9, pp. 1427–1452, 1993.

[21] J. Bergenholtz and N. J. Wagner, "Formation of AOT/brine multilamellar vesicles," *Langmuir*, vol. 12, no. 13, pp. 3122–3126, 1996.

[22] J. Zipfel, J. Berghausen, P. Lindner, and W. Richtering, "Influence of shear on lyotropic lamellar phases with different membrane defects," *The Journal of Physical Chemistry B*, vol. 103, no. 15, pp. 2841–2849, 1999.

[23] M. E. Cates and S. T. Milner, "Role of shear in the isotropic-to-lamellar transition," *Physical Review Letters*, vol. 62, no. 16, p. 1856, 1989.

[24] S. Ramaswamy, "Shear-induced collapse of the dilute lamellar phase," *Physical Review Letters*, vol. 69, no. 1, p. 112, 1992.

[25] V. Rathee, R. Krishnaswamy, A. Pal, V. A. Raghunathan, M. Impéror-Clerc, B. Pansu, and A. K. Sood, "Reversible shear-induced crystallization above equilibrium freezing temperature in a lyotropic surfactant system," *Proceedings of the National Academy of Sciences, USA*, vol. 110, no. 37, pp. 14849–14854, 2013.

[26] E. Mendes and S. V. G. Menon, "Vesicle to micelle transitions in surfactant mixtures induced by shear," *Chemical Physics Letters*, vol. 275, no. 5-6, pp. 477–484, 1997.

[27] C. E. Fairhurst, M. C. Holmes, and M. S. Leaver, "Shear Alignment of a Rhombohedral Mesh Phase in Aqueous Mixtures of a Long Chain Nonionic Surfactant," *Langmuir*, vol. 12, no. 26, pp. 6336–6340, 1996.

[28] "The supplemental material is given in the section VII below, which includes; estimation of defect's volume, shear-study of low concentrated L_α^D of CPC-SHN-water system, equilibrium study of the $R\bar{3}m$, Rheo-SALS during the flow curve of $R\bar{3}m$, and supplemental Figures.."

[29] B. Struth, K. Hyun, E. Kats, T. Meins, M. Walther, M. Wilhelm, and G. Grubel, "Observation of new states of liquid crystal 8CB under nonlinear shear conditions as observed via a novel and unique rheology/small-angle x-ray scattering combination," *Langmuir*, vol. 27, no. 6, pp. 2880–2887, 2011.

[30] M. Goulian and S. T. Milner, "Shear alignment and instability of smectic phases," *Physical Review Letters*, vol. 74, no. 10, p. 1775, 1995.

[31] A. Wunenburger, A. Colin, J. Leng, A. Arnéodo, and D. Roux, "Oscillating viscosity in a lyotropic lamellar phase under shear flow," *Physical Review Letters*, vol. 86, no. 7, p. 1374, 2001.

[32] R. Bruinsma and Y. Rabin, "Shear-flow enhancement and suppression of fluctuations in smectic liquid crystals," *Physical Review A*, vol. 45, no. 2, p. 994, 1992.

[33] P. Boltenhagen, O. D. Lavrentovich, and M. Kleman, "Focal conic domains with positive Gaussian curvature and saddle-splay rigidity of smectic La phases," *Physical Review A*, vol. 46, no. 4, p. R1743, 1992.

[34] S. S. Funari and G. Rapp, "A continuous topological change during phase transitions in amphiphile/water systems," *Proceedings of the National Academy of Sciences, USA*, vol. 96, no. 14, pp. 7756–7759, 1999.

[35] L. Yang and H. W. Huang, "A rhombohedral phase of lipid containing a membrane fusion intermediate structure," *Biophysical Journal*, vol. 84, no. 3, pp. 1808–1817, 2003.

[36] I. W. Hamley, "Structure and flow behaviour of block copolymers," *Journal of Physics: Condensed Matter*, vol. 13, no. 33, p. R643, 2001.

[37] J. Berghausen, J. Zipfel, P. Lindner, and W. Richtering, "Shear-induced orientations in a lyotropic defective lamellar phase," *EPL (Europhysics Letters)*, vol. 43, no. 6, p. 683, 1998.

[38] J. Zipfel, F. Nettesheim, P. Lindner, T. D. Le, U. Olsson, and W. Richtering, "Cylindrical intermediates in a shear-induced lamellar-to-vesicle transition," *EPL (Europhysics Letters)*, vol. 53, no. 3, p. 335, 2001.

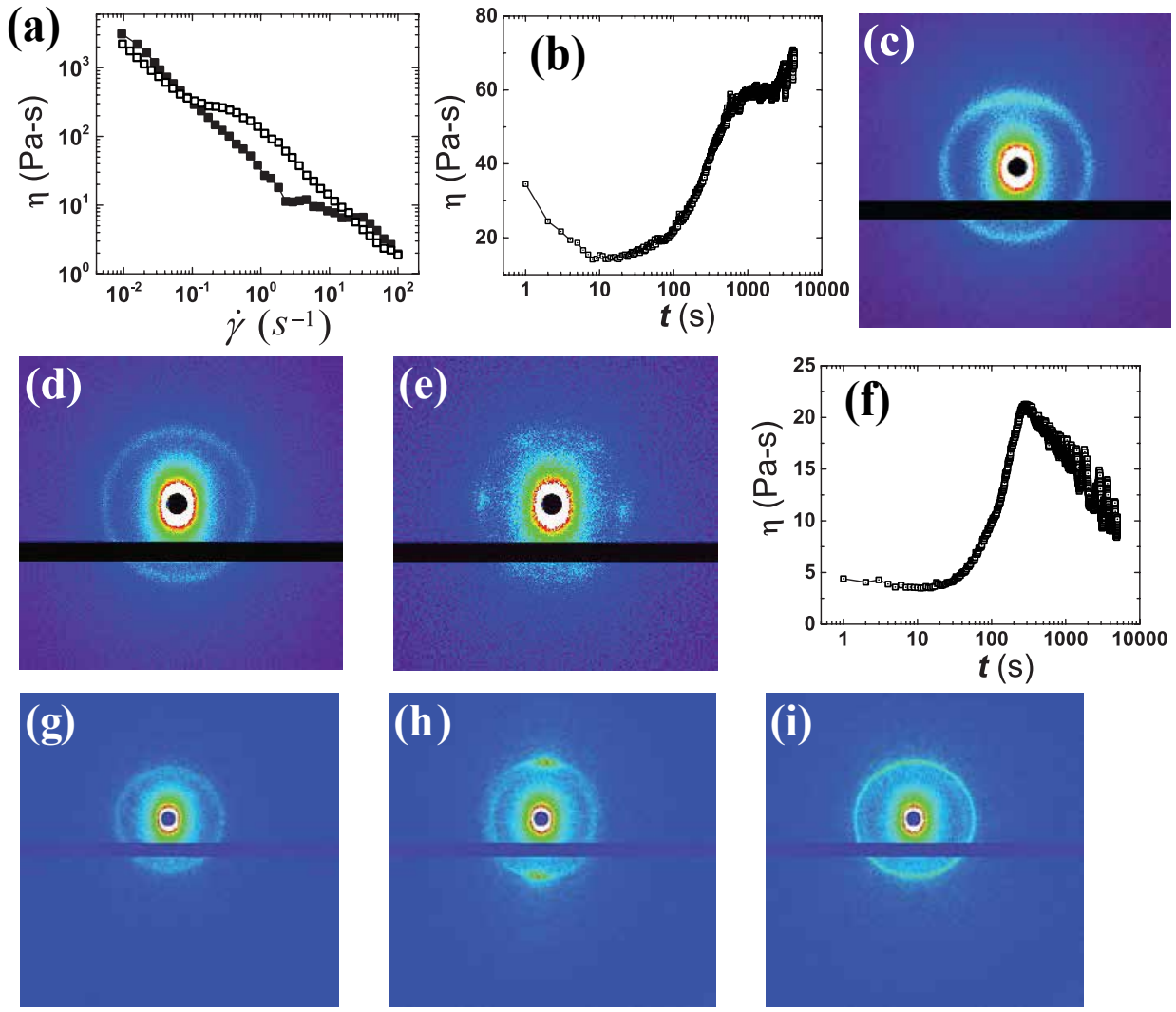

FIG. 1. Shear rate controlled flow curve; (a) viscosity (η) vs shear rate ($\dot{\gamma}$) of the random mesh phase (L_α^D) formed in CTAB-SHN-water system, $\phi = 0.40$ and $\alpha = 1$, in PP geometry with 30 s waiting time at each data point. Filled symbol and empty symbol represent increasing and decreasing $\dot{\gamma}$ respectively. Stress relaxation measurements at $\dot{\gamma} = 10$ s^{-1}, with the same system and geometry; for $\phi = 0.30$, (b) viscosity (η) vs time (t) and the corresponding X-ray diffraction patterns at (c) $t = 0$ s, (d) $t = 100$ s, (e) $t = 1000$ s. For $\phi = 0.40$, (f) η vs t and the corresponding diffraction patterns at (g) $t = 0$ s, (h) $t = 10$ s, (i) $t = 1000$ s.

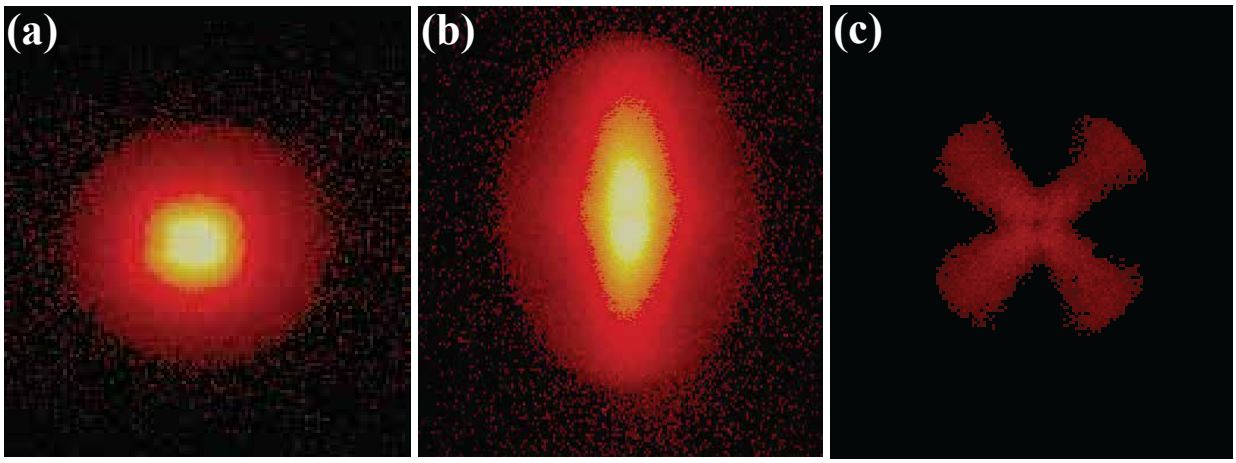

FIG. 2. Small-Angle Light Scattering patterns under stress relaxation measurement similar to Fig. 1(f), namely, $\phi = 0.40$, $\alpha = 1$, $\dot{\gamma} = 10\ \mathrm{s}^{-1}$: for (a) $t = 0$ s, (b) $t = 10$ s, (c) $t = 500$ s.

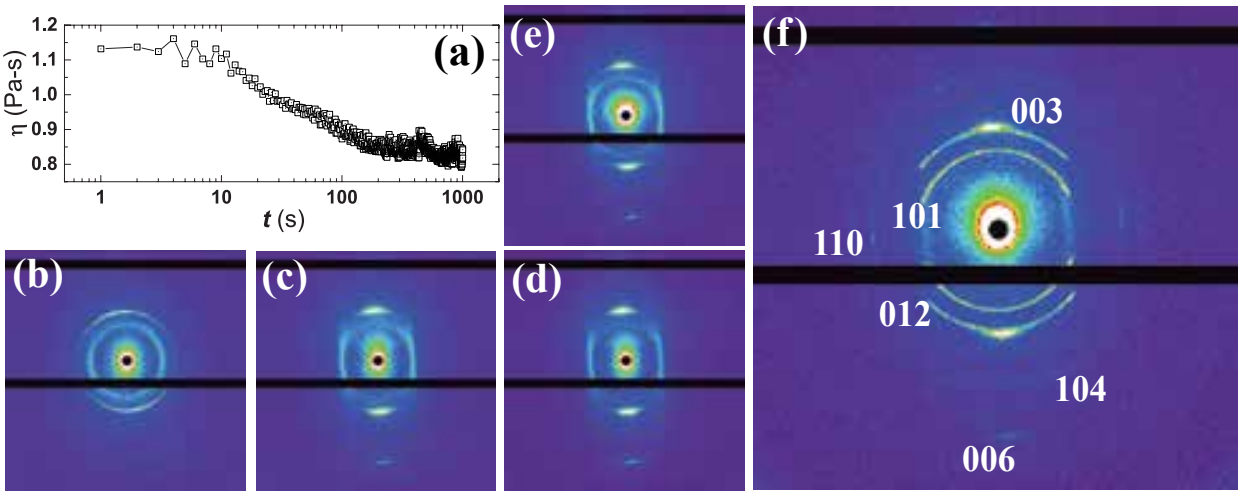

FIG. 3. Stress relaxation measurement at $\dot{\gamma} = 50\ \mathrm{s}^{-1}$ in PP geometry, CTAB-SHN-water system ($\alpha = 1$, $\phi = 0.50$). (a) η vs t and the corresponding X-ray diffraction patterns at (b) $t = 0$ s, (c) $t = 50$ s, (d) $t = 125$ s, (e) $t = 515$ s, (f) $t = 850$ s. R$\bar{3}$m lattice planes are marked near the observed Bragg rings in (f).

TABLE I. Indexing the X-ray diffraction patterns shown in Fig. 3, obtained by shearing the L_α^D phase (CTAB-SHN-water system, $\alpha = 1$, $\phi = 0.5$) at $\dot{\gamma} = 50$ s^{-1}. The average in-plane nano-pore separation (d_d) and the lamellar d-spacing (d_l) are marked. For the patterns at $t = 515$ s and at $t = 850$ s revealing the shear-induced R$\bar{3}$m phase, the calculated d-spacings (d_{cal}) are obtained using the relation $(1/d)^2 = (4/3)(h^2 + hk + k^2)/a^2 + l^2/c^2$ with the condition $-h + k + l = 3n$, where n is an integer. The calculated unit cell parameters $a = 8.68$ nm, $c = 15.93$ nm are same for both.

t (s)	d_{obs} (nm)	hkl	d_{cal} (nm)	error (%)	intensity
0	7.67(d_d)			0	broad
	5.49(d)			0	very strong
	2.76($d/2$)			0.5	strong
50	7.92(d_d)			0	broad
	5.31(d)			0	very strong
	2.68($d/2$)			0.9	strong
515	7.79(d_d)			0	broad
	6.80	101	6.80	0	very strong
	5.49	012	5.47	0.4	strong
	5.31	003	5.31	0	very strong
	4.39	110	4.34	1.1	weak
	2.68	006	2.66	0.8	strong
850	7.79(d_d)			0	broad
	6.80	101	6.80	0	very strong
	5.49	012	5.47	0.4	very strong
	5.31	003	5.31	0	very strong
	4.39	110	4.34	1.1	strong
	3.77	021	3.66	2.9	weak
	3.53	104	3.52	0.3	strong
	3.02	015	2.93	3	weak
	2.66	006	2.66	0	strong

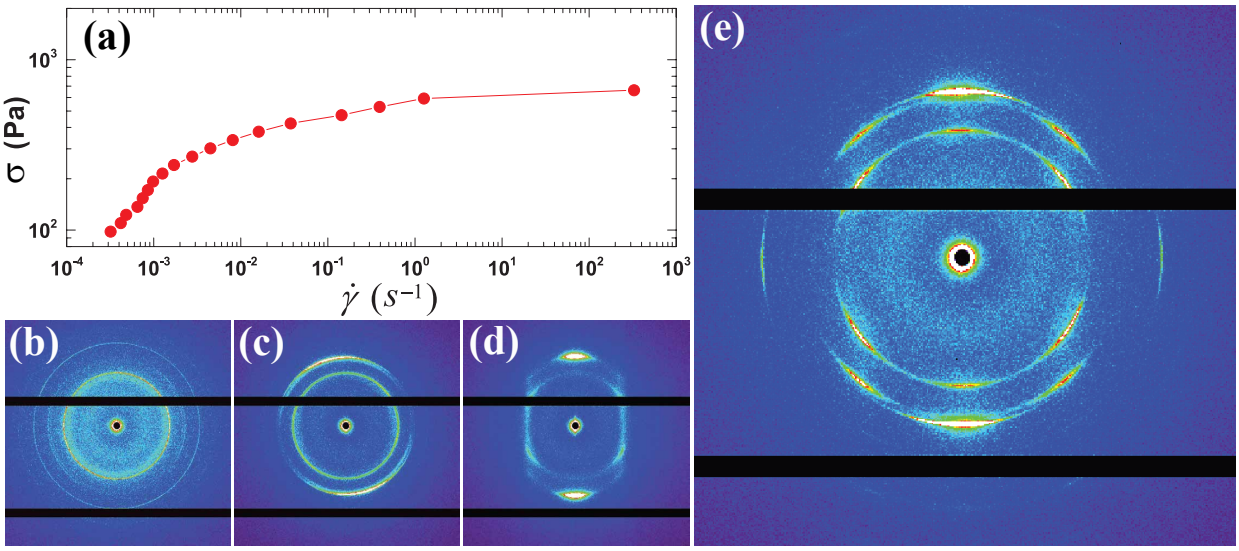

FIG. 4. Stress controlled flow curve with 200 s waiting time at each data point in PP geometry for CTAB-SHN-water system, $\alpha = 1$, $\phi = 0.53$: (a) σ vs $\dot{\gamma}$, X-ray diffraction patterns for (b) $\sigma = 0$ Pa, (c) $\sigma = 470$ Pa, (d) $\sigma = 590$ Pa, (e) $\sigma = 660$ Pa.

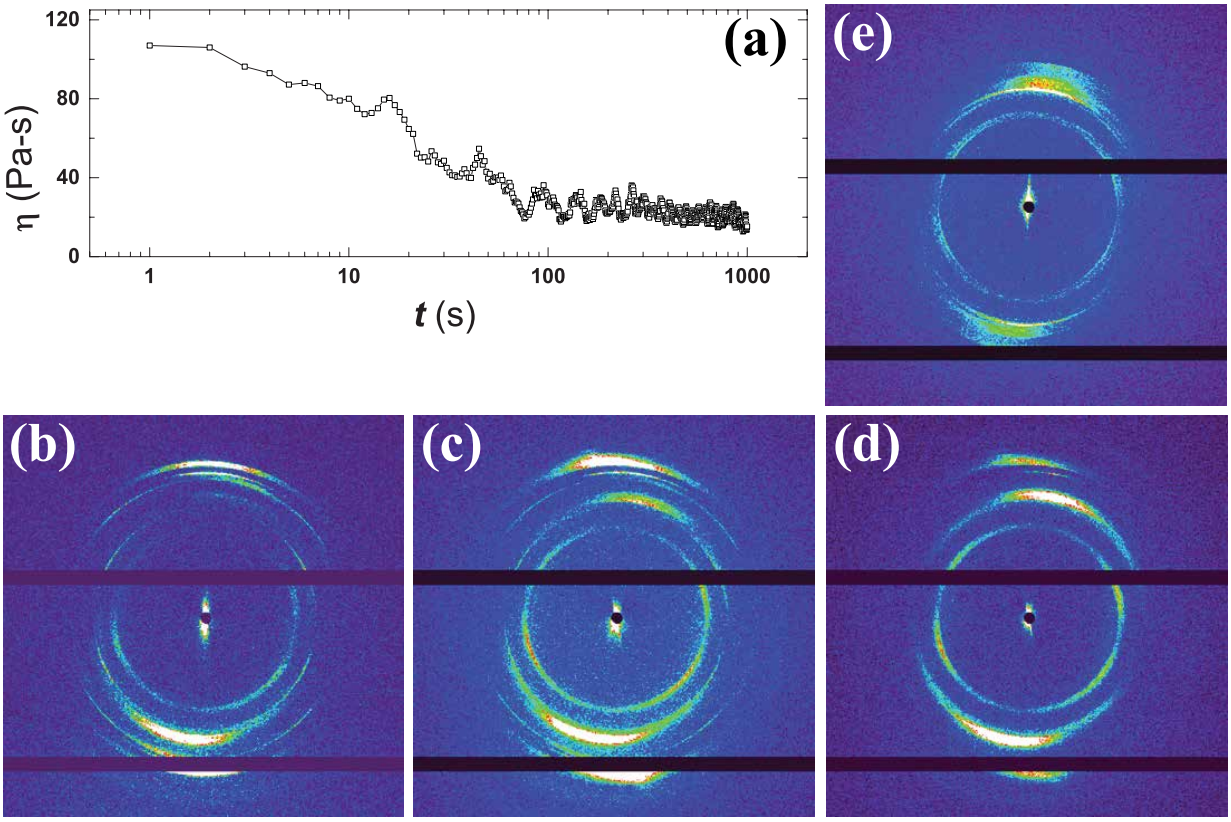

FIG. 5. Stress relaxation of R$\bar{3}$m phase (CTAB-SHN-water system, $\alpha = 1$, $\phi = 0.53$) at $\dot{\gamma} = 1$ s^{-1} in Couette geometry: (a) η vs t and the corresponding X-ray diffraction patterns obtained during 700 s $\leq t \leq$ 850 s with incident X-ray beam at different distances (g_x) from the inner static cylinder at (b) $g_x = 0.6$ mm, (c) $g_x = 0.8$ mm, (d) $g_x = 1.0$ mm, (e) $g_x = 1.2$ mm.

TABLE II. Indexing the X-ray diffraction patterns shown in Fig. 4 for different σ.

σ (Pa)	d_{obs} (nm)	hkl	d_{cal} (nm)	error (%)	intensity	unit cell (nm)
0	7.00	101	7.00	0	very strong	$a = 8.95$
	5.65	012	5.62	0.5	weak	$c = 16.32$
	5.44	003	5.44	0	strong	
	4.47	110	4.47	0	very strong	
	3.78	021	3.77	0.3	strong	
	2.81	024	2.81	0	weak	
	2.28	220	2.24	1.8	weak	
470	7.00	101	7.00	0	very strong	$a = 8.96$
	5.61	012	5.60	0.2	weak	$c = 16.20$
	5.40	003	5.40	0	strong	
	4.47	110	4.48	0.2	very strong	
	3.78	021	3.77	0.3	strong	
	3.59	104	3.59	0	strong	
	2.97	015	2.99	0.7	weak	
	2.69	006	2.70	0.4	weak	
590	7.00	101	7.00	0	very strong	$a = 9.00$
	5.61	012	5.57	0.7	strong	$c = 15.93$
	5.31	003	5.31	0	very strong	
	4.47	110	4.50	0.7	strong	
	2.66	006	2.66	0	strong	
660	7.00	101	7.00	0	very strong	$a = 8.98$
	5.57	012	5.59	0.4	very strong	$c = 16.05$
	5.35	003	5.35	0	very strong	
	4.45	110	4.49	0.9	very strong	
	3.78	021	3.78	0	weak	
	3.55	104	3.57	0.6	strong	
	2.96	015	2.97	0.3	weak	
	2.67	006	2.68	0.4	very strong	

TABLE III. Indexing the X-ray diffraction patterns shown in Fig. 5(b) for $g_x = 0.6$ mm. Peaks are fitted to set of two R$\bar{3}$m with calculated unit cell parameters as $a1 = 10.58$ nm, $c1 = 18.60$ nm (1^{st} R$\bar{3}$m) and $a2 = 8.50$ nm, $c2 = 14.25$ nm (2^{nd} R$\bar{3}$m).

	1^{st} R$\bar{3}$m		2^{nd} R$\bar{3}$m			
d_{obs} (nm)	hkl	d_{cal} (nm)	hkl	d_{cal} (nm)	error (%)	intensity
8.22	101	8.22			0	very strong
6.54	012	6.53	101	6.54	0.2, 0	very strong
6.20	003	6.20			0	very strong
5.22	110	5.29			1.3	very strong
5.10			012	5.12	0.4	very strong
4.75			003	4.75	0	very strong
2.93	006	3.10	113	3.17	5.5, 7.6	strong

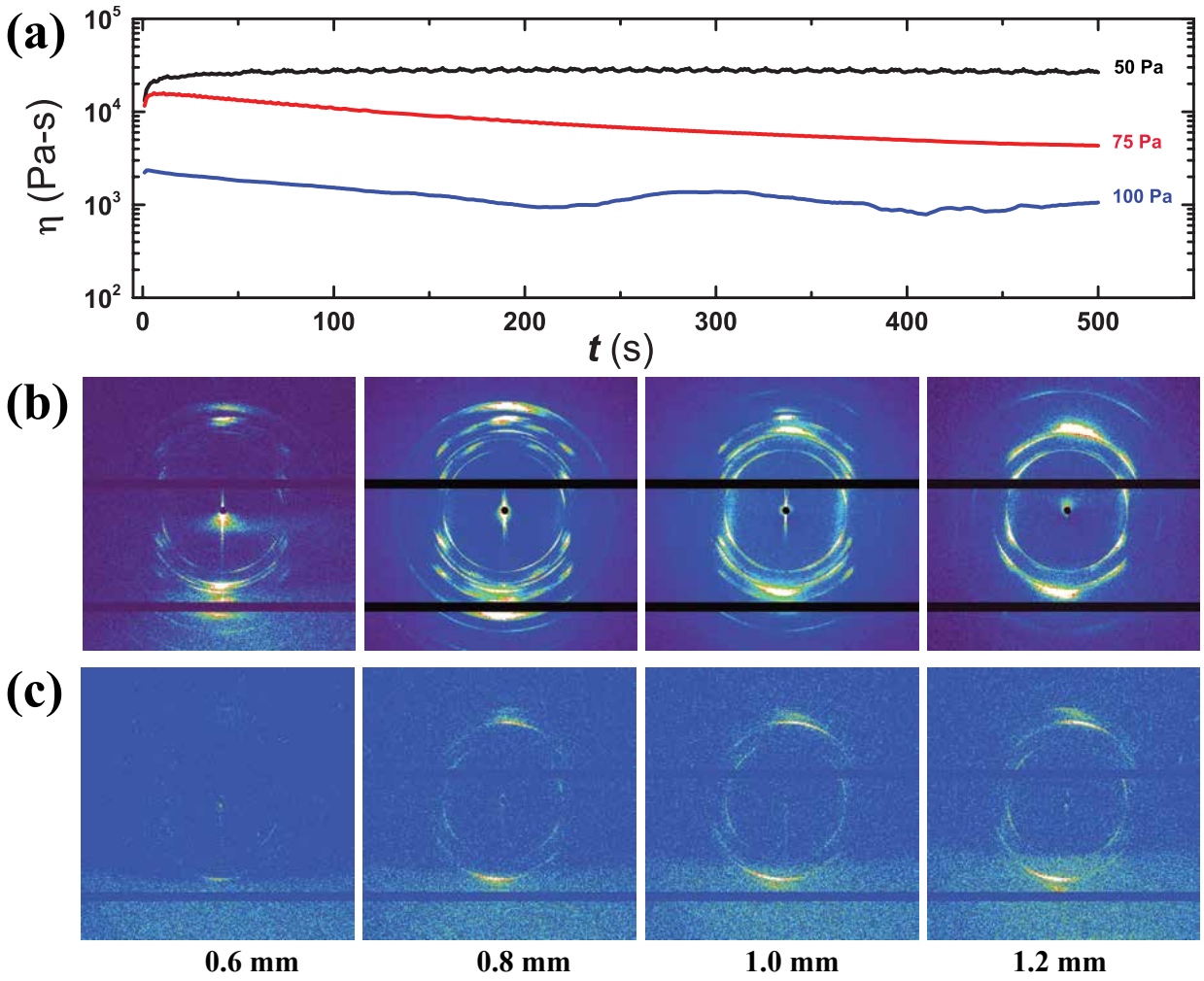

FIG. 6. Shear rate relaxation for R$\bar{3}$m phase in CTAB-SHN-water system, $\alpha = 1$, $\phi = 0.53$ with Couette geometry: (a) η vs t at different applied σ. X-ray diffraction patterns for different g_x are shown for (b) $\sigma = 100$ Pa and (c) $\sigma = 75$ Pa. For each measurement a fresh sample was loaded and the SAXS was done during 300 s $\leq t \leq$ 450 s.

TABLE IV. Indexing the X-ray diffraction patterns corresponding to $g_x = 0.8$ mm for different σ shown in Fig. 6. For $\sigma = 100$ Pa, peaks are fitted to set of two R$\bar{3}$m phases with calculated unit cell parameters as $a1$, $c1$ (1^{st} R$\bar{3}$m) and $a2$, $c2$ (2^{nd} R$\bar{3}$m). Lamellar peaks are marked by d and $d/2$. Peak intensity vs, s, and w represent very strong, strong, and weak respectively.

		1^{st} R$\bar{3}$m		2^{nd} R$\bar{3}$m				
σ	d_{obs}	hkl	d_{cal}	hkl	d_{cal}	error	intensity	unit cell
(Pa)	(nm)		(nm)		(nm)	(%)		(nm)
75	6.86	101	6.86			0	s	$a = 8.84$
	5.44	012	5.44			0	w	$c = 15.48$
	5.16	003	5.16			0	vs	
100	6.73	101	6.73			0	vs	$a1 = 8.65$
	5.65			101	5.65	0	vs	$c1 = 15.36$
	5.35	012	5.36			0.19	vs	$a2 = 7.43$
	5.12	003	5.12			0	vs	$c2 = 11.79$
	4.42			012	4.35	1.58	vs	
	4.34	110	4.32			0.46	w	
	3.93			003	3.93	0	vs	
	3.76(d)						vs	
	3.72			110	3.72	0	vs	
	3.38	202	3.37			0.30	vs	
	2.82	015	2.84			0.70	s	
	2.62	006	2.56			2.29	vs	
	2.54	030	2.50			1.58	vs	
	2.21			015	2.21	0	s	
	1.98			006	1.96	1.01	s	
	1.86($d/2$)	401	1.86			0	w	

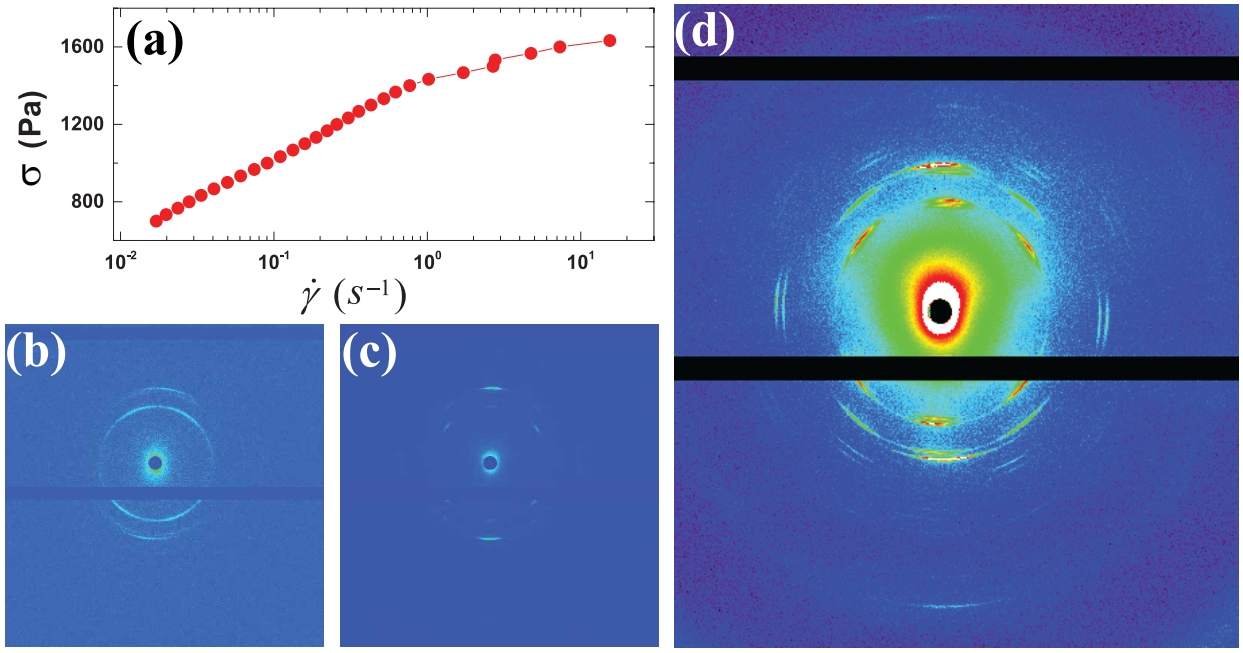

FIG. 7. (a) Stress-controlled flow curve for R$\bar{3}$m phase formed in CTAB-SHN-water at $\alpha = 1$, $\phi = 0.6$. X-ray diffraction patterns for (b) $\sigma = 1133$ Pa, (c) $\sigma = 1400$ Pa, (d) $\sigma = 1600$ Pa.

TABLE V. Indexing the X-ray diffraction patterns shown in Fig. 7(d). Peaks are fitted to set of two R$\bar{3}$m phases with calculated unit cell parameters as $a1 = 8.13$ nm, $c1 = 13.80$ nm (1^{st} R$\bar{3}$m) and $a2 = 7.69$ nm, $c2 = 13.80$ nm (2^{nd} R$\bar{3}$m).

	1^{st} R$\bar{3}$m		2^{nd} R$\bar{3}$m			
d_{obs} (nm)	hkl	d_{cal} (nm)	hkl	d_{cal} (nm)	error (%)	intensity
6.27	101	6.27			0	very strong
6.00			101	6.00	0	very strong
4.82			112	4.79	0.6	very strong
4.60	003	4.60	003	4.60	0, 0	very strong
4.09	110	4.06			0.7	weak
3.89			110	3.85	1.0	weak
3.48	021	3.41			2.0	strong
3.26			021	3.24	0.6	strong
3.08			104	3.06	0.6	strong
2.30	006	2.30			0	strong

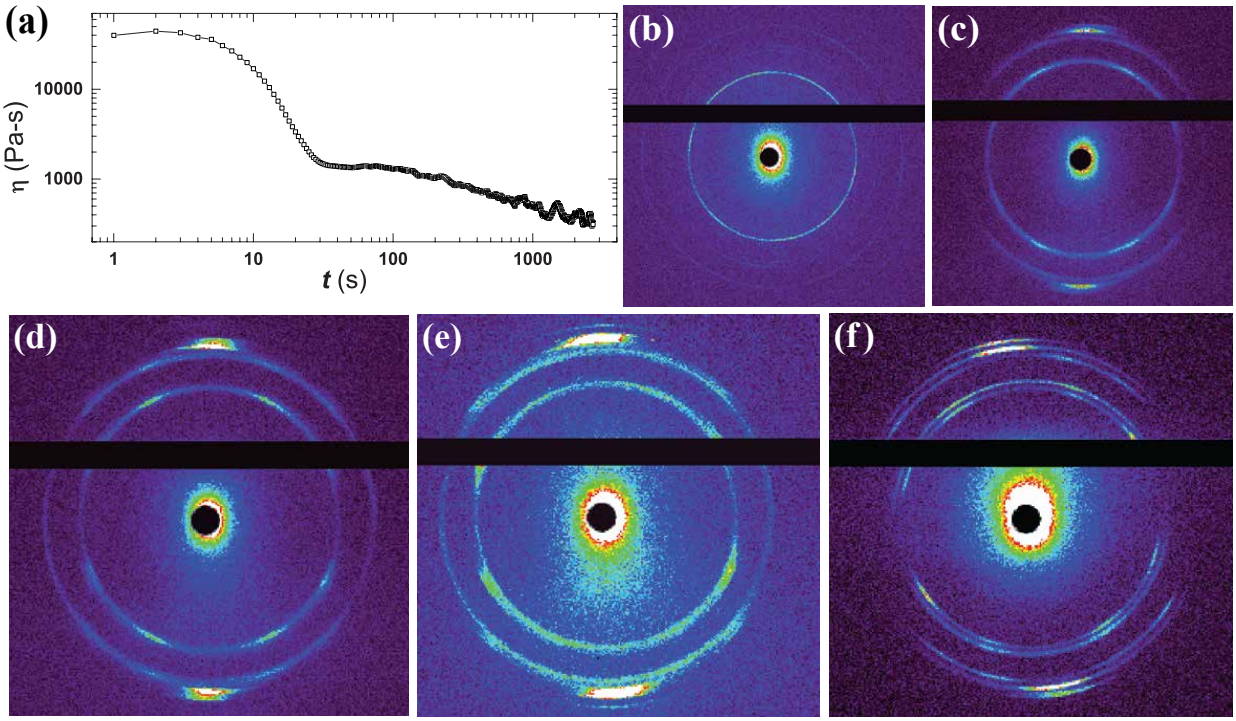

FIG. 8. (a) η vs time of CTAB-SHN-water system, $\alpha = 1$, $\phi = 0.60$ at $\dot{\gamma} = 1\ \mathrm{s}^{-1}$ in PP geometry. X-ray diffraction patterns at (b) $t = 0$ s, (c) $t = 70$ s, (d) $t = 75$ s, (e) $t = 80$ s, (f) $t = 500$ s. The buckling of R$\bar{3}$m can be observed.

TABLE VI. Indexing the X-ray diffraction patterns shown in Fig. 8(f). Peaks are fitted to set of two R$\bar{3}$m phases with calculated unit cell parameters as $a1 = 7.76$ nm, $c1 = 13.80$ nm (1^{st} R$\bar{3}$m) and $a2 = 7.38$ nm, $c2 = 13.17$ nm (2^{nd} R$\bar{3}$m).

	1^{st} R$\bar{3}$m		2^{nd} R$\bar{3}$m			
d_{obs} (nm)	hkl	d_{cal} (nm)	hkl	d_{cal} (nm)	error (%)	intensity
6.04	101	6.04			0	very strong
5.75			101	5.75	0	very strong
4.83	012	4.81			0.4,0	very strong
4.60	003	4.60	012	4.59	0,0.22	very strong
4.39			003	4.39	0	very strong
3.08	104	3.07	021	3.11	0.32,0.97	weak
2.29	006	2.30	024	2.29	0.43, 0	strong

VII. SUPPLEMENTAL MATERIAL

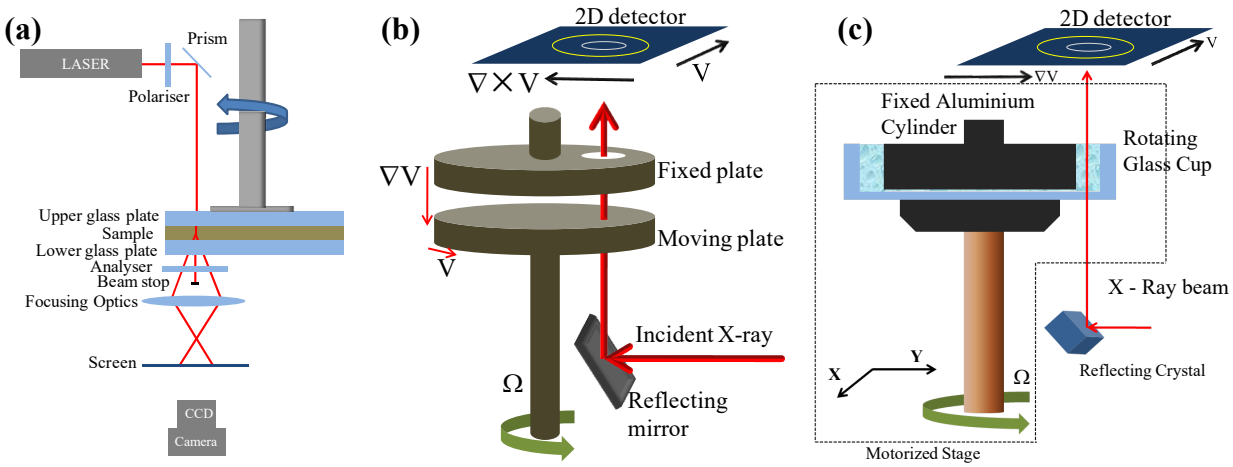

FIG. S1. (a) Schematic of rheo-SALS setup. (b) Rheo-SAXS setup (static) with PP vespel geometry. (c) With Couette glass geometry, rheo-SAXS setup on a motorized stage to do the X-ray scan across the gap by varying the distance (d_x) of the X-ray from the inner static cylinder.

A. Estimation of defect's volume using the right rhombic prism model [Fig. S2]

Using the surfactant weight fraction ϕ and the density ratio f_ρ, it can be shown from the Fig. S2 that if V_w is the total volume occupied by water and V_s is the total volume occupied by surfactant then we have,

$$\Rightarrow \frac{V_w}{V_s} = \frac{f_\rho}{\phi}; \quad \text{where} \quad f_\rho = \frac{\rho_s}{\rho_w} \quad \text{and} \quad \phi = \frac{W_s}{W_w} \tag{1}$$

$$\Rightarrow \frac{(\sqrt{3}/2)d_d^2(d_l - 2r) + \pi R^2 2r}{((\sqrt{3}/2)d_d^2 - \pi R^2)2r} = \frac{f_\rho}{\phi} \tag{2}$$

$$\Rightarrow \pi R^2 2r(f_\rho + \phi) = (\sqrt{3}/2)d_d^2(2r f_\rho - (d_l - 2r)\phi) \tag{3}$$

$$\Rightarrow \text{defect volume} \sim \pi R^2 2r = \frac{(\sqrt{3}/2)d_d^2(2r f_\rho - (d_l - 2r)\phi)}{(f_\rho + \phi)} \tag{4}$$

$$\tag{5}$$

The Table S1 shows the calculated defect volume for different surfactant concentration using the measured in-plane defect correlation length (d_d) and the bilayer periodicity (d_l) of L_α^D phase or using the measured lattice parameters of $R\bar{3}m$ phase at equilibrium.

TABLE S1. **Taken value of r = 2.1 nm (from literature) and f_ρ = 1.03 (measured).**

system	ϕ	the phase	d_d or a (nm)	d_l or c/3 (nm)	defect volume (nm)
CTAB-SHN-Water	0.40	L_α^D	6.93	7.30	90.17
	0.50	L_α^D	7.67	5.49	123.14
	0.53	$R\bar{3}m$	8.95	5.44	163.90
	0.60	$R\bar{3}m$	8.30	4.70	148.03
CPCl-SHN-Water	0.55	L_α^D	6.50	5.13	88.74

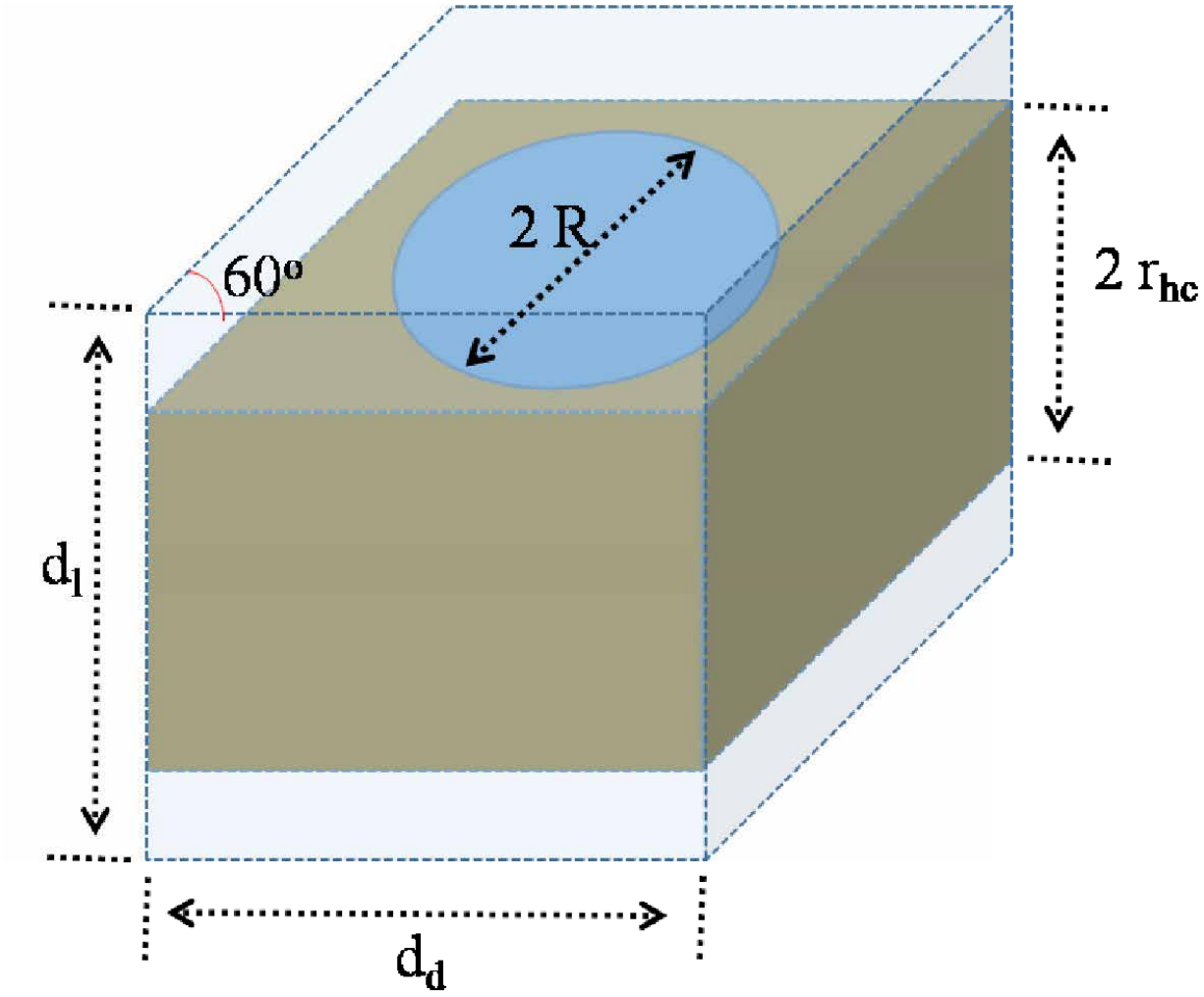

FIG. S2. right rhombic prism of sides d_d, d_d with angle 60° and height d_l. Surfactant layer of thickness 2r has a cylinder of diameter 2R at the centre filled with water. Top and bottom space out side the surfactant is filled with water.

B. shear-induced L_α^D phase to R$\bar{3}$m phase transition in CPC-SHN-water system

With PP geometry, shear-induced L_α^D phase to R$\bar{3}$m phase transition in the CPC-SHN-water system ($\alpha = 0.5$, $\phi = 0.55$) is observed during the stress relaxation at $\dot{\gamma} = 50$ s^{-1} [Fig. S3(a)]. In equilibrium, as shown in Fig. S3(b), the X-ray diffraction pattern reveals an unoriented lamellar with d-spacing of 5.13 nm, coexisting with the diffuse peak from nano-pores with 6.50 nm liquid-like average correlation length. A nearly a-oriented diffraction pattern is obtained at $t \sim 10$ s, with the average orientation of lamellar peaks along $\mathbf{q}_\perp$ [Fig. S3(c)]. The azimuthal spread of the lamellar peak decreases upon further shearing and at $t \sim 20$ s [Fig. S3(d)], a sharp peak comes up after the diffuse peak indicating 3D ordering of nano-pores getting established under shear similar to the observation in the case of CTAB-SHN-water system (discussed in the main text). After $t = 30$ s, other higher order peaks start appearing [Fig. S3(e)]. All the sharp reflections obtained at $t \sim 40$ s [Fig. S3(f)], can be indexed to two R$\bar{3}$m phases with lattice parameters $a1 = 8.39$ nm; $c1 = 14.79$ nm; $a2 = 8.27$ nm; $c2 = 14.28$ nm [Table S2].

TABLE S2. Indexing the X-ray diffraction pattern of the shear-induced R$\bar{3}$m phase [Fig. S3(f)], obtained by shearing the L_α^D phase (CPC-SHN-water system, $\alpha = 0.5$, $\phi = 0.55$) at $\dot{\gamma} = 50$ s^{-1}. Peaks are fitted to set of two R$\bar{3}$m phases with the calculated unit cell parameters as $a1 = 8.39$ nm, $c1 = 14.79$ nm (1^{st} R$\bar{3}$m) and $a2 = 8.27$ nm, $c2 = 14.28$ nm (2^{nd} R$\bar{3}$m).

	1^{st} R$\bar{3}$m		2^{nd} R$\bar{3}$m			
d_{obs} (nm)	hkl	d_{cal} (nm)	hkl	d_{cal} (nm)	error (%)	intensity
6.52	101	6.52			0	strong
6.40			101	6.40	0	strong
5.06	012	5.18	012	5.06	2.3, 0	very strong
4.93	003	4.93			0	very strong
4.76			003	4.76	0	very strong
3.20	113	3.19	202	3.20	0.3, 0	weak
3.10			113	3.12	0.6	weak
2.53	006	2.47	122	2.53	2.4, 0	weak

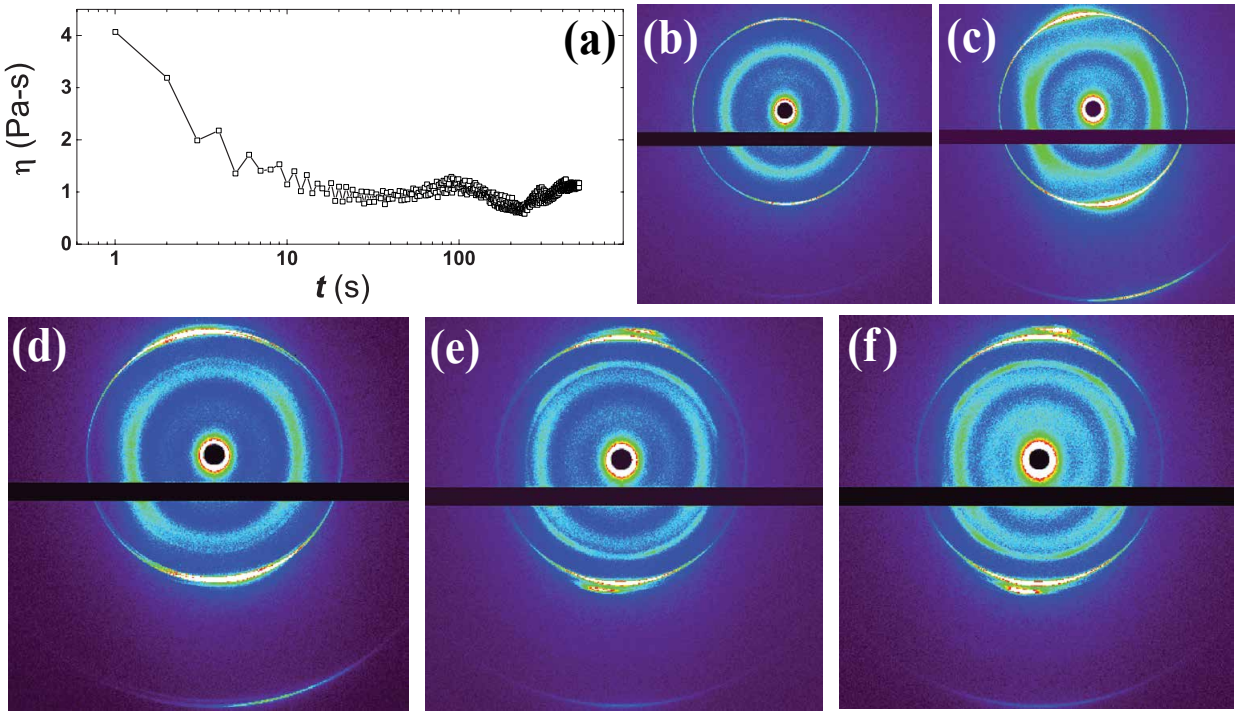

FIG. S3. With PP geometry, shear-induced L_α^D phase to $R\bar{3}m$ phase transition in CPC-SHN-water system ($\alpha = 0.5$, $\phi = 0.55$) is observed during stress relaxation measurement at $\dot{\gamma} = 50\ s^{-1}$. (a) η vs t plot and the corresponding X-ray diffraction patterns at (b) $t = 0$ s, (c) $t = 10$ s, (d) $t = 20$ s, (e) $t = 30$ s, (f) $t = 40$ s are shown.

C. Equilibrium study of the rhombohedral mesh phase using Rheo-SALS and Rheo-SAXS setups

Figure S4 shows the SALS and the SAXS patterns from the ordered mesh phase (weight fraction $\phi = 0.53$ and $\alpha = 1$) at equilibrium just before the rheology measurements. The equilibrium patterns are azimuthally isotropic with respect to the central beam spot and independent of the geometry in use, a typical signature of randomly oriented crystalline domains. The positions of the SAXS rings in q-space can be indexed to a rhombohedral unit cell having the space group symmetry R$\bar{3}$m.

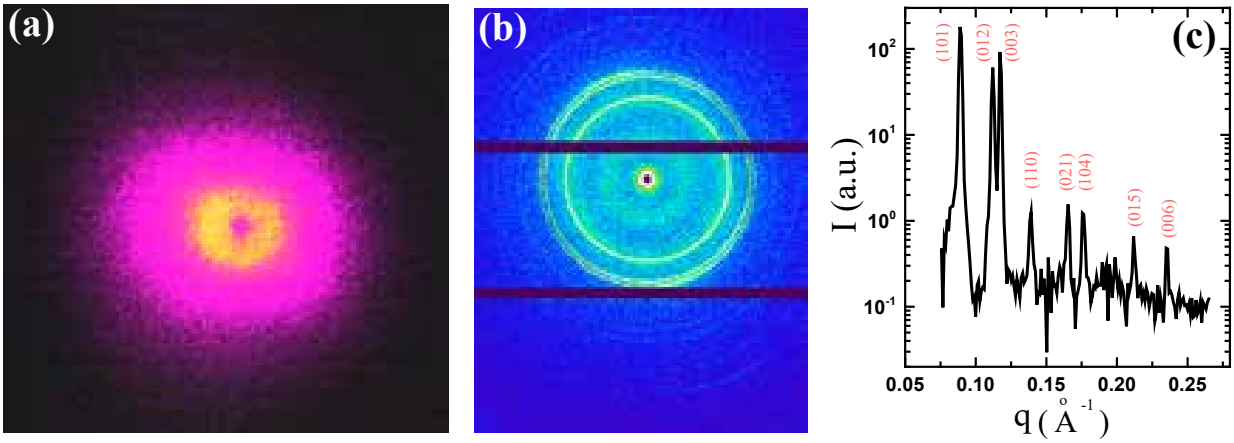

FIG. S4. (a) Small angle light scattering (SALS) pattern and (b) small angle X-ray scattering (SAXS) pattern from the rhombohedral phase formed by CTAB-SHN-Water ternary system prepared with $\alpha = 1$, $\phi = 0.53$ at 30° C are shown. These patterns were captured while the samples were resting between the rheometer plates. (c) Intensity vs wave vector (q) plot of the SAXS shows the positions of the isotropic rings in q-space. Fitted lattice panes (having R$\bar{3}$m symmetry) are indicated.

D. Rheo-SALS during the shear stress controlled flow curve measurement with $R\bar{3}m$ phase

The rheo-SALS measurements were performed separately in PP glass geometry with VH configuration. Figure S5 shows the shear stress controlled flow curve where the shear stress was varied from 100 Pa to 1000 Pa with a waiting time of 200 s at each point. The unaligned scattering pattern [Fig. S5(a)] transforms to a partially aligned at $\sigma = 200\ Pa$ [Fig. S5(b)] and then shows a-oriented bilayers, bilayer planes parallel to the velocity-velocity gradient plane at 300 Pa [Fig. S5(c)]. Interestingly, at 600 Pa and above a star-like pattern appears [Fig. S5(d)].

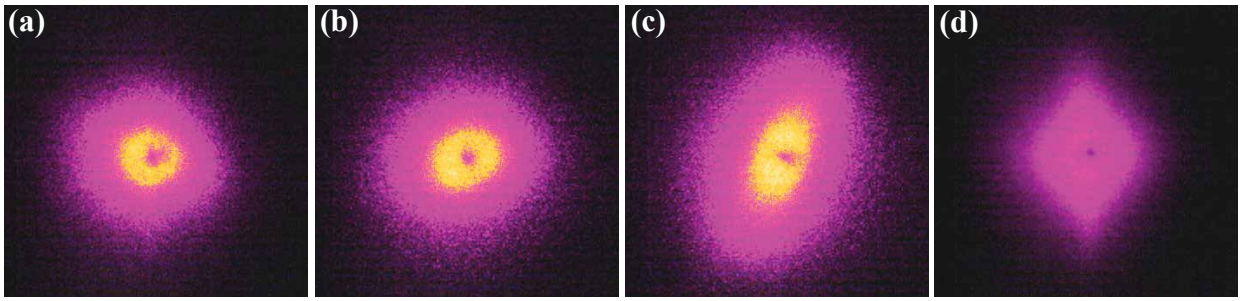

FIG. S5. SALS patterns obtained during the shear stress controlled flow curve measurement, are shown for different σ: (a) 0Pa, (b) 200Pa, (c) 300Pa, (d) 600Pa.

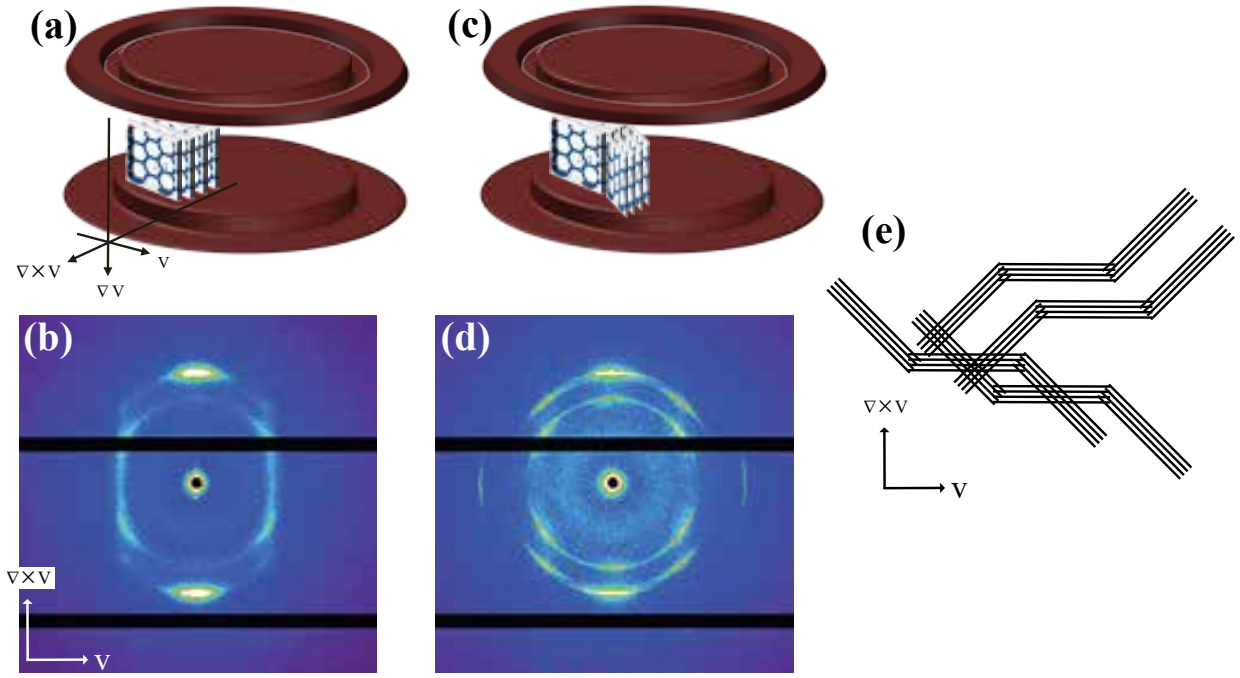

FIG. S6. (a) Schematic of a-orientated R$\bar{3}$m in PP geometry is shown, and (b) the corresponding observed SAXS pattern with four arcs in (101), (012) rings is shown. (c) Buckling of R$\bar{3}$m is depicted, and (d) the corresponding pattern with six arcs in (101), (012) rings is shown. (e) Top view of the buckled state of R$\bar{3}$m is shown, where each bilayer is represented by a straight line. Different directions of the geometry are indicated.